

BCS-BEC crossover in a $(t_{2g})^4$ Excitonic Magnet

Nitin Kaushal,^{1,2} Rahul Soni,^{1,2} Alberto Nocera,³ Gonzalo Alvarez,⁴ and Elbio Dagotto^{1,2}

¹*Department of Physics and Astronomy, The University of Tennessee, Knoxville, Tennessee 37996, USA*

²*Materials Science and Technology Division, Oak Ridge National Laboratory, Oak Ridge, Tennessee 37831, USA*

³*Department of Physics and Astronomy and Stewart Blusson Quantum Matter Institute,
University of British Columbia, Vancouver, B.C., Canada, V6T 1Z1*

⁴*Computational Sciences and Engineering Division and Center for Nanophase Materials Sciences,
Oak Ridge National Laboratory, Oak Ridge, Tennessee 37831, USA*

(Dated: February 1, 2022)

The condensation of spin-orbit-induced excitons in t_{2g}^4 electronic systems is attracting considerable attention. In the large Hubbard U limit, antiferromagnetism was proposed to emerge from the Bose-Einstein Condensation (BEC) of triplons ($J_{\text{eff}} = 1$). In this publication, we show that even for the weak and intermediate U regimes, the spin-orbit exciton condensation is possible leading also to staggered magnetic order. The canonical electron-hole excitations (excitons) transform into local triplon excitations at large U , and this BEC strong coupling regime is smoothly connected to the intermediate U excitonic insulator region. We solved the degenerate three-orbital Hubbard model with spin-orbit coupling (λ) in one-dimensional geometry using the Density Matrix Renormalization Group, while in two-dimensional square clusters we use the Hartree-Fock approximation (HFA). Employing these techniques, we provide the full λ vs U phase diagrams for both one- and two-dimensional lattices. Our main result is that at the intermediate Hubbard U region of our focus, increasing λ at fixed U the system transitions from an incommensurate spin-density-wave metal to a Bardeen-Cooper-Schrieffer (BCS) excitonic insulator, with coherence length r_{coh} of $\mathcal{O}(a)$ and $\mathcal{O}(10a)$ in $1d$ and $2d$, respectively, with a the lattice spacing. Further increasing λ , the system eventually crosses over to the BEC limit (with $r_{\text{coh}} \ll a$).

I. INTRODUCTION

Excitonic condensation has attracted considerable attention for over half a century, since its early theoretical prediction [1]. An exciton is a bound state of an electron-hole pair. This composite particle resembles the Cooper pair of superconductors and follows hard-core bosonic statistics. Early work involving semiconductors showed that in the weak-coupling limit (small U), near the semimetal to semiconductor transition and depending on the excitonic binding energy and the band gap, the system can become unstable against the formation of multiple excitons [2, 3] and this can lead to a condensation into a BCS-like macroscopic state called Excitonic Insulator. This BCS wavefunction smoothly transforms into a BEC state, if the gap between the bands increases at fixed Hubbard repulsion U . The phenomenon of excitonic condensation in strongly correlated systems can also lead to a BEC-like Excitonic Insulator in the strong coupling limit (large U). This regime also attracted considerable theoretical investigations [4–6] and has been studied using perturbation theory at large U , where the hopping amplitude t is the small parameter.

The extended Falicov-Kimball model has been used often as a minimal theoretical model to investigate the above discussed physics [7–9]. Only recently, the more realistic, but also more difficult, three-orbital Hubbard models were explored to study excitonic condensation [10–13]. Due to the theoretical progress, on the experimental side there have been some studies showing reliable signatures of the excitonic condensate in real materials such as in a transition metal dichalcogenide [14],

Ta_2NiSe_5 [15], and in bilayer systems [16, 17]. To increase our understanding of this interesting Excitonic Insulator it is important to find additional candidate materials and additional theoretical models where the excitonic condensation occurs and can be studied in detail. Recently, it was recognized that materials with strong spin-orbit coupling can also provide a new avenue for the study of excitons and excitonic condensation [18, 19]. For example, Sr_2IrO_4 , with Ir^{4+} ions and filling $n = 5$ electrons per Iridium ion (t_{2g}^5), is a celebrated material due to the presence of long-range antiferromagnetic ordering in quasi two-dimensional layers, as in the case of superconducting cuprates [20]. Recent resonant inelastic X-ray scattering (RIXS) experiments on Sr_2IrO_4 have reported the presence of excitons as an excitation at approximately 0.5 – 0.6 eV [21–23]. RIXS experiments on one-dimensional stripes of Sr_2IrO_4 have also shown the presence of excitons at nearly the same energy [24]. These excitons are present in spin-orbit entangled states, hence known as *spin-orbit excitons*.

Another promising avenue to study excitonic condensates induced by spin-orbit coupling involves the t_{2g}^4 case, which is the focus of the present paper. Theoretically, it has been predicted that the three-orbital Hubbard model with a degenerate t_{2g} space and in the LS coupling limit ($U \gg t, \lambda$) can lead to the BEC state of triplons (singlet-triplet excitations) [25–27]. We will show that these triplon excitations are low-energy manifestations of spin-orbit excitons. Cluster Dynamical Mean Field Theory (DMFT) calculations have also supported similar findings [10, 11], although it is difficult to distinguish between BCS and BEC states in the small clusters used.

A recent computational study of the ground state of a one-dimensional spin-orbit coupled three-orbital Hubbard model in a non-degenerate (tetragonal) t_{2g} space using the numerically-exact density matrix renormalization group (DMRG) also reported a phase with staggered spin-orbit excitonic correlations [12]. All the above mentioned studies reveal an antiferromagnetic ordering accompanying the excitonic condensate. The t_{2g}^4 case is relevant for materials with Ir^{5+} ions and other $4d/5d$ transition metal oxides with the same doping $n = 4$. The presence of triplon condensation was initially discussed for double perovskite materials, such as Sr_2YIrO_6 and Ba_2YIrO_6 with a $5d^4$ configuration [28–33], but later on RIXS experiments showed that the bandwidth of triplon excitations is not sufficiently large in comparison to λ to develop condensation [34]. It should be remarked that recent RIXS experiments on Ca_2RuO_4 suggests that this compound could be a candidate material for excitonic magnetism [35], and *ab-initio* calculations have reached the same conclusion [36].

To investigate the spin-orbit excitonic condensation, this paper uses a simple degenerate three-orbital Hubbard model. Using numerically exact DMRG simulations on one-dimensional chains, we show that even in the intermediate Hubbard repulsion regime ($U/W \approx 1$) an excitonic condensation is induced accompanied by antiferromagnetic ordering. This regime is stabilized by increasing sufficiently λ starting at the incommensurate spin-density wave metallic region of $\lambda = 0$. This numerical result of a spin-orbit excitonic condensate at intermediate U/W cannot be understood using large U perturbation theories. Moreover, in two-dimensional ($2d$) lattices, by using the Hartree-Fock Approximation (HFA), we have also found a similar excitonic insulator phase in both the weak and intermediate U/W regimes. As our main result, we show that there is a BCS-BEC crossover inside the excitonic condensate phase, both in the $1d$ and $2d$ lattices we studied. The BCS limit of the excitonic insulator occurs at intermediate U/W (and also for weak U/W in $2d$), and by increasing λ (at fixed U/W) the BEC state is reached. The previously known BEC state present at large U/W , due to the condensation of triplons, is here shown to be smoothly connected to the BCS excitonic insulator of intermediate and weak U . At strong coupling, in the non-magnetic phase at large λ , higher than needed for the excitonic magnetic phase, these electron-hole pair excitations transform into low-energy triplons ($\Delta J_{\text{eff}} = 1$) and higher-energy quintuplons ($\Delta J_{\text{eff}} = 2$) excitations and those triplons condense on decreasing λ . We provide numerical evidence for this triplon condensation using DMRG by calculating the excitonic pair-pair susceptibility. We also provide the full λ vs U phase diagrams for $1d$ and $2d$ lattices using the many-body techniques discussed above.

The organization of this paper is as follows. In Sec. II, the model used and the computational methodology are presented. We discuss the atomic limit of the Hamiltonian in Sec. III. In Sec. IV, the main results are shown.

In particular, in Sec. IVA, the results on $1d$ lattices using the DMRG technique are presented. In Sec. IVB, the results on $2d$ lattices using HFA are displayed to further support our main proposal of a BCS-BEC crossover in the model studied. In Sec. V, we discuss the overall results and present our conclusions.

II. MODEL AND METHOD

For the study presented in this publication, we used a degenerate three-orbital Hubbard model. The Hamiltonian has three primary terms: the tight-binding kinetic energy, the standard on-site multiorbital Hubbard interaction, and the on-site spin-orbit coupling (SOC): $H = H_K + H_{\text{int}} + H_{\text{SOC}}$. The tight-binding term is written as

$$H_K = \sum_{\langle i,j \rangle, \sigma, \gamma, \gamma'} t_{\gamma\gamma'} (c_{i\sigma\gamma}^\dagger c_{j\sigma\gamma'} + \text{H.c.}). \quad (1)$$

The hopping amplitudes $t_{\gamma\gamma'}$ connect only nearest-neighbor lattice sites (in both the $1d$ chain and $2d$ square lattices). As discussed earlier, here we use degenerate orbitals, that is, $t_{\gamma\gamma'} = \delta_{\gamma\gamma'} t$. In some cases we fixed $t = 0.5$ for simplicity but most of our results are expressed in terms of dimensionless ratios, such as U/W or λ/t . The total bandwidth is $W = 4.0|t|$ and $8.0|t|$ for the $1d$ and $2d$ lattices, respectively. The above mentioned orbitals – labeled as 0, 1, and 2 – could be associated respectively to the d_{yz} , d_{xz} , and d_{xy} orbitals, namely the t_{2g} sector. The on-site multiorbital Hubbard interaction term in the Hamiltonian consists of the standard several components

$$\begin{aligned} H_{\text{int}} = & U \sum_{i, \gamma} n_{i\uparrow\gamma} n_{i\downarrow\gamma} + (U' - J_H/2) \sum_{i, \gamma < \gamma'} n_{i\gamma} n_{i\gamma'} \\ & - 2J_H \sum_{i, \gamma < \gamma'} \mathbf{S}_{i\gamma} \cdot \mathbf{S}_{i\gamma'} + J_H \sum_{i, \gamma < \gamma'} \left(P_{i\gamma}^\dagger P_{i\gamma'} + \text{h.c.} \right). \end{aligned} \quad (2)$$

In the equation above, $\mathbf{S}_{i\gamma} = \frac{1}{2} \sum_{\alpha, \beta} c_{i\alpha\gamma}^\dagger \sigma_{\alpha\beta} c_{i\beta\gamma}$ represents the spin at orbital γ and lattice site i , while $n_{i\gamma}$ is the electronic density operator also at orbital γ and site i . The first two terms are the intra- and inter-orbital electronic repulsion, respectively. The Hund coupling is contained in the third term, which favors the ferromagnetic alignment of the spins at different orbitals and the same site. Finally, the $P_{i\gamma} = c_{i\downarrow\gamma} c_{i\uparrow\gamma}$ operator in the fourth term (pair-hopping) is the pair annihilation operator that arises from the matrix elements of the “ $1/r$ ” Coulomb repulsion as in the early studies of Kanamori. We used the standard relation $U' = U - 2J_H$ due to rotational invariance, and we fix $J_H = U/4$ for all the calculations as employed widely in previous efforts [12, 13, 37–39].

The SOC term is

$$H_{\text{SOC}} = \lambda \sum_{i, \gamma, \gamma', \sigma, \sigma'} \langle \gamma | \mathbf{L}_i | \gamma' \rangle \cdot \langle \sigma | \mathbf{S}_i | \sigma' \rangle c_{i\sigma\gamma}^\dagger c_{i\sigma'\gamma'}, \quad (3)$$

where the coupling λ is the SOC strength.

Using the model described above, we performed calculations on one-dimensional chains employing the DMRG technique [40, 41] for various system lengths, such as $L = 16, 24$, and 32 sites. We have used up to 1600 states for the DMRG process and have maintained a truncation error below 10^{-8} throughout the finite algorithm sweeps. We used the corrected single-site DMRG algorithm [42] with correction $a = 0.001-0.008$, and performed 35 to 40 finite sweeps to gain proper convergence depending on the system size. After this convergence, we calculated the spin-structure factor $S(q)$, orbital-structure factor $L(q)$, excitonic momentum distribution function $\Delta_{m=1/2}(q)$, and coherence length r_{coh} . With the information gathered from all these observables, we constructed the phase diagram. To calculate spectral functions with the DMRG, we have used the correction vector method [43], with the Krylov-space approach [44]. We obtain the single-particle spectral function $A(q, \omega)$ and the excitonic pair-pair susceptibility $\Delta_{m=1/2}(q, \omega)$. These frequency-dependent observables require heavy computational time, and multiple compute nodes. In our DMRG calculations, we target the total J_{eff}^z of the system to reduce the computational cost [12]. Details of the Hartree-Fock calculations are discussed in Sec. IVB below.

III. ATOMIC LIMIT

Before describing our results for chains and planes, we will discuss in detail the atomic limit of our Hamiltonian to introduce to the readers particular aspects of the t_{2g}^4 system. The magnetic properties in the $n = 4$ case with a finite spin-orbit coupling are fascinating because in the atomic limit the ground state is a singlet having $J_{eff} = 0$ for any finite value of λ/U . Only at $\lambda = 0$, the $J_{eff} = 0, 1, 2$ states are degenerate in the ground state manifold. Figure 1(a) shows the energies of the excited states relative to the $J_{eff} = 0$ ground state. The evolution of magnetic moments and occupations in the single-particle spin-orbit (j_{eff}, m) states is displayed in Fig. 1(b). Note that j_{eff} is the effective total angular momentum of the electron and m is the projection along the z -axis. Sometimes the quantum number j_{eff} will be denoted as j , if it appears in subindex.

The jj coupling limit ($\lambda/U \gg 1$) can be understood by diagonalizing the spin-orbit coupling term. The transformation between the t_{2g} orbitals and the j_{eff} basis is given by (site i index dropped)

$$\begin{bmatrix} a_{\frac{3}{2}, \frac{3}{2}} \\ a_{\frac{3}{2}, -\frac{3}{2}} \\ a_{\frac{1}{2}, -\frac{3}{2}} \end{bmatrix} = \begin{bmatrix} \frac{is}{\sqrt{2}} & \frac{1}{\sqrt{2}} & 0 \\ \frac{s}{\sqrt{6}} & \frac{i}{\sqrt{6}} & \frac{2}{\sqrt{6}} \\ \frac{-s}{\sqrt{3}} & \frac{-i}{\sqrt{3}} & \frac{1}{\sqrt{3}} \end{bmatrix} \begin{bmatrix} c_{\sigma yz} \\ c_{\sigma xz} \\ c_{\bar{\sigma} xy} \end{bmatrix}, \quad (4)$$

where s is 1(-1) when σ is $\uparrow(\downarrow)$ and $\bar{\sigma} = -\sigma$. The H_{SOC}

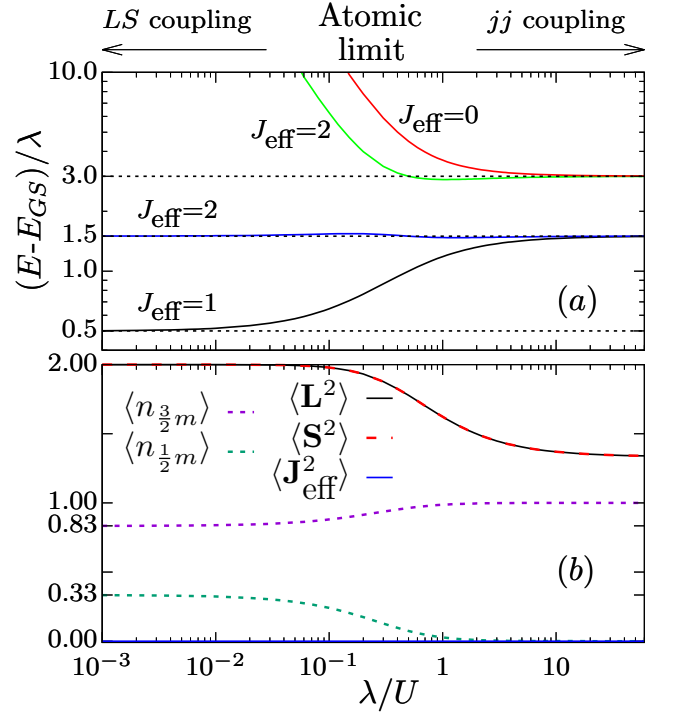


FIG. 1. Panel (a) shows the energies of excited states with respect to the ground state energy denoted by E_{GS} . In panel (b), the occupation in the (j, m) states and the local moments are shown. For the plots in this figure, $U = 1$ is fixed and λ varies. The results illustrate the evolution from the LS coupling to the jj coupling regimes.

term in the j_{eff} basis becomes

$$\begin{aligned} H_{SOC} = \sum_i \frac{\lambda}{2} & (-a_{i, \frac{3}{2}, \frac{3}{2}}^\dagger a_{i, \frac{3}{2}, \frac{3}{2}} - a_{i, \frac{3}{2}, -\frac{1}{2}}^\dagger a_{i, \frac{3}{2}, -\frac{1}{2}} \\ & - a_{i, \frac{3}{2}, -\frac{3}{2}}^\dagger a_{i, \frac{3}{2}, -\frac{3}{2}} - a_{i, \frac{3}{2}, \frac{1}{2}}^\dagger a_{i, \frac{3}{2}, \frac{1}{2}} \\ & + 2a_{i, \frac{1}{2}, \frac{1}{2}}^\dagger a_{i, \frac{1}{2}, \frac{1}{2}} + 2a_{i, \frac{1}{2}, -\frac{1}{2}}^\dagger a_{i, \frac{1}{2}, -\frac{1}{2}}). \end{aligned} \quad (5)$$

The expression above clearly shows that for $n = 4$ the ground state has all $j_{eff} = 3/2$ states fully occupied, and all $j_{eff} = 1/2$ states empty (i.e. $|GS\rangle_{jj} = a_{\frac{3}{2}, \frac{3}{2}}^\dagger a_{\frac{3}{2}, -\frac{3}{2}}^\dagger a_{\frac{3}{2}, \frac{1}{2}}^\dagger a_{\frac{3}{2}, -\frac{1}{2}}^\dagger |0\rangle$) leading to a total $J_{eff} = 0$. The first excited state is located with a gap $3\lambda/2$, as shown in Fig. 1(a). Also it can be checked that $jj < GS|L^2|GS\rangle_{jj} < GS|S^2|GS\rangle_{jj} = 4/3$. On the other hand, in the LS coupling limit only one-third fraction of the $(j_{eff} = 1/2, m)$ states is occupied, with both the magnitudes of S and L being 1.

The information presented above in the atomic limit is relevant for cases with $U/W \ll 1$ and a finite spin-orbit coupling, to find out in which limit the system is located. For example, recently compounds with isolated $RuCl_6$ octahedra exhibited a single-ion physics with a non-magnetic $J_{eff} = 0$ state [45]. Next, we will discuss our results for the $1d$ and $2d$ lattices where the presence of kinetic energy can drive the system away from this

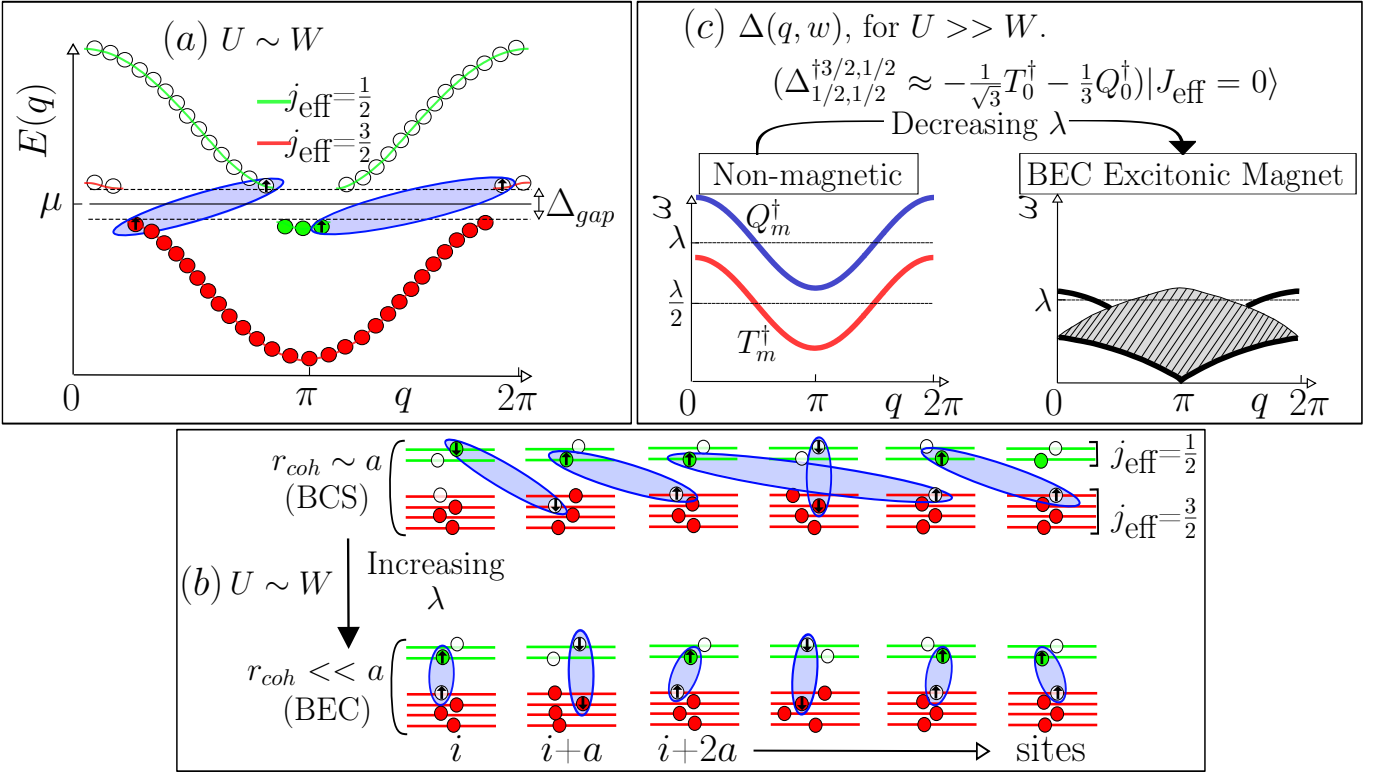


FIG. 2. Visual representation of the main results of this publication, all supported by actual DMRG and Hartree Fock calculations. In (a), the single-particle excitations of the $j_{\text{eff}} = 3/2$ and $j_{\text{eff}} = 1/2$ bands are shown at intermediate U , where near the chemical potential the gap opens due to the formation of excitons (note electron and hole have the same m). The $j_{\text{eff}} = 3/2$ and $j_{\text{eff}} = 1/2$ bands open gaps near momentum $q \approx 0$ and $q \approx \pi$, respectively. In (b), the real-space perspective of the excitonic state (at intermediate U) is shown, where the exciton's mean radius (characterized by the coherence length) decreases by increasing λ . In (c), the excitonic condensation mechanism in the strong coupling limit is depicted. The local exciton creation operator leads to the creation of both a triplon and a quintuplon when acting on $|J_{\text{eff}} = 0\rangle$. In the presence of kinetic energy, i.e. including the tight-binding term, the triplon and quintuplon excitations gain bandwidths, and decreasing λ leads to the Bose-Einstein condensation of the triplon component.

atomic limit, leading to magnetic ordering.

IV. DMRG RESULTS IN ONE DIMENSION

This section presents the DMRG numerical results for one-dimensional chains, and discuss their implications. Figure 2 visually summarizes our conclusions. Within our numerical accuracy, we observed that the excitonic condensation starts at intermediate Hubbard correlation strength $U \approx \mathcal{O}(W)$. This condensation of excitons opens a gap in the $j_{\text{eff}} = 3/2$ and $j_{\text{eff}} = 1/2$ bands at momentum $q = 0$ and $q = \pi$, respectively, as shown in Fig. 2(a). A similar perspective for the gap opening near the Fermi level by excitonic condensation was discussed in early research for semiconductors [1]. At intermediate U , we noticed the excitons condense at finite momentum π and in the triplet channel (for details see Supplementary [46]). We also noticed that increasing λ (concomitantly adjusting U to remain inside the excitonic condensation region) decreases the coherence length (r_{coh}) of

electron-hole pairs from approximately one lattice spacing (a) to a much smaller number $r_{\text{coh}} \ll a$, resembling the BCS-BEC crossover. Although in the extreme BCS limit r_{coh} can be as large as hundreds of lattice spacings, outside our resolution, in our finite and one dimensional system we only found a robust indication for a maximum r_{coh} of approximately $1.0a$ which definitely is different from the BEC limit $r_{\text{coh}} \ll a$. Confirming that indeed we found a BCS-BEC crossover at intermediate U , we performed mean-field calculations on $2d$ lattices (Sec. V), where we found r_{coh} as large as $\mathcal{O}(10a)$ in the BCS limit.

We have also found clear distinctions between the exciton-exciton correlation decay in the BCS and BEC limits in one-dimensional chains. It can be shown that the excitonic operator $\Delta_{1/2,m}^{\dagger 3/2,m}$ in the single-atom LS coupling limit can be written in terms of triplon and quintuplon excitations (see Supplementary [46]), corresponding, respectively, to $T_n^\dagger |J_{\text{eff}}^z = 0, \mathbf{J}_{\text{eff}} = 0\rangle = |n, 1\rangle$, and $Q_l^\dagger |J_{\text{eff}}^z = 0, \mathbf{J}_{\text{eff}} = 0\rangle = |l, 2\rangle$, where $n \in \{\pm 1, 0\}$

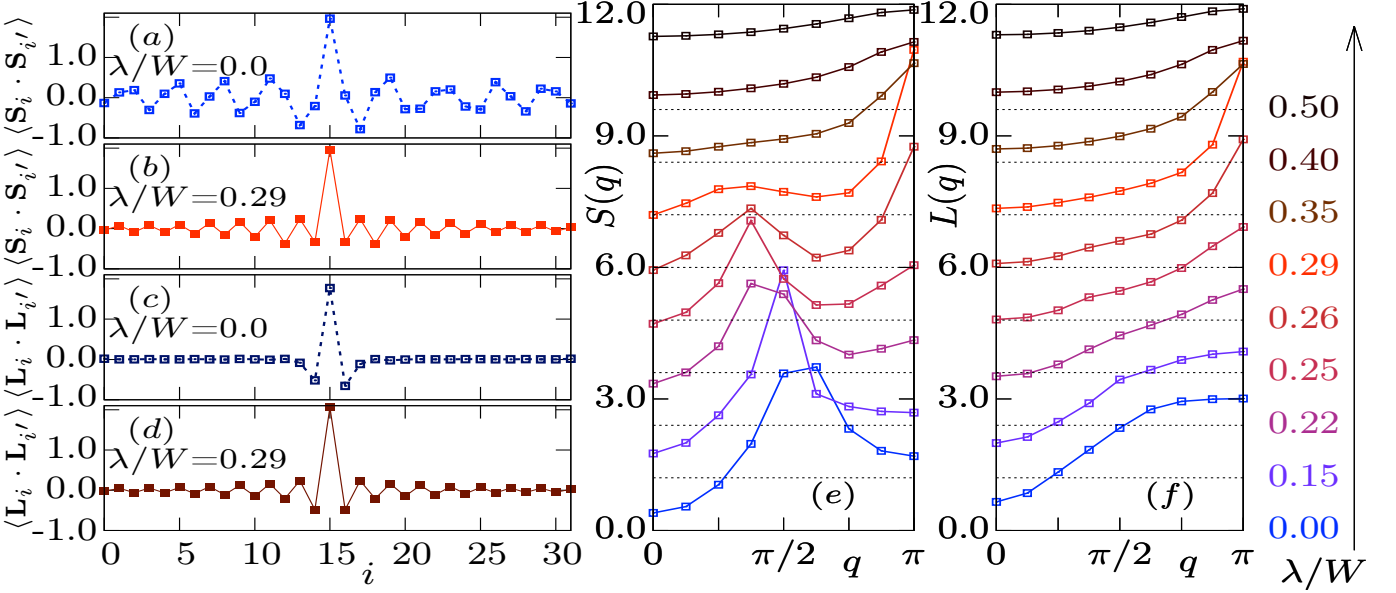


FIG. 3. DMRG results at fixed $U/W = 2$. Panels (a) and (b) show the real-space spin-spin correlations at $\lambda/W = 0$ and $\lambda/W = 0.29$, respectively. In (c) and (d), the real-space orbital-orbital correlations are shown at $\lambda/W = 0.0$ and $\lambda/W = 0.29$, respectively. The spin structure factor $S(q)$ and orbital structure factors $L(q)$ are shown in panels (e) and (f), respectively, for various values of λ . For panels (a,b,c,d) the system size $L = 32$ and one site is fixed at the center i.e. $i' = 15$. A system size $L = 16$ is used for panels (e,f).

and $l \in \{\pm 2, \pm 1, 0\}$. By calculating the pair-pair susceptibility of excitons $\Delta(q, \omega)$ for one-dimensional chains, in the non-magnetic phase present in the strong coupling limit, we found bands of triplon and quintuplon excitations, with minima at $q = \pi$ but both bands are gapped. We noticed that decreasing λ drives the system to the BEC state, where $\Delta(q, \omega)$ has clear signatures of gapped triplon and quintuplon excitations only near $q = 0$ but mainly a continuum of excitations at other momenta above the Goldstone-like modes emerging from $q = \pi$, as sketched in Fig. 2(c).

A. Magnetic properties and staggered excitonic correlations

Now let us discuss the results for magnetism in one-dimensional chains. We choose $U/W = 2.0$ and $U/W = 10.0$ as representative points for the intermediate and strong coupling regions, respectively. First, consider the intermediate coupling region where at $\lambda = 0$ we found an incommensurate spin-density wave (IC-SDW) via the spin-spin correlation $\langle \mathbf{S}_i \cdot \mathbf{S}_{i'} \rangle$ together with an exponential fast decay in the orbital-orbital correlation $\langle \mathbf{L}_i \cdot \mathbf{L}_{i'} \rangle$, as shown in Figs. 3(a,c). Block magnetic states, as discussed in [37] and [39], do not appear in our model at $\lambda = 0$. Increasing λ drives the system towards antiferromagnetism with staggered spin-spin and orbital-orbital correlations, as shown in Figs. 3(b,d). For additional confirmation, we show the spin structure factor $S(q) = (1/L) \sum_{i,j} e^{iq(j-i)} \langle \mathbf{S}_i \cdot \mathbf{S}_j \rangle$, and the orbital struc-

ture factor $L(q) = (1/L) \sum_{i,j} e^{iq(j-i)} \langle \mathbf{L}_i \cdot \mathbf{L}_j \rangle$ for various λ values. As λ increases, the spin structure factor $S(q)$ in Fig. 3(e) indicates that the incommensurate peak shifts to lower q values. The antiferromagnetic tendencies, shown by the $q = \pi$ peak, starts only near $\lambda = 0.22W$, and on further increasing λ the $q = \pi$ peak grows and the incommensurate peak is reduced. At larger λ 's the $S(q = \pi)$ peak decreases as the system transitions into the non-magnetic state. The orbital structure factor $L(q)$ displays similar behaviour at $q = \pi$. $L(q)$ starts with a flat plateau near $q = \pi$, then $L(q = \pi)$ grows when increasing λ , and eventually the $L(q = \pi)$ peak vanishes for very large λ , as shown in Fig. 3(f).

In the strong coupling limit, and at $\lambda = 0$, the spins align ferromagnetically and orbital-orbital correlations show a “+ - - + - -” pattern, depicted by peaks at momentum $q = 0$ and near $q = 2\pi/3$ in $S(q)$ and $L(q)$, respectively (see Fig. 4). Note that recent DMRG calculations on the low-energy $S=1$ and $L=1$ model also showed similar results in the orbital correlations [47] at $\lambda = 0$. We noticed that as λ increases, the system enters into the phase where orbital ordering becomes staggered, as shown by a peak at $q = \pi$ for $\lambda = 0.05W$ in Fig. 4(a). However, the spin ordering is dominantly ferromagnetic with small antiferromagnetic tendencies leading to a small peak at $q = \pi$ [Fig. 4(b) for $\lambda = 0.05W$]. Further increasing λ , both $L(q = \pi)$ and $S(q = \pi)$ grow while $S(q = 0)$ decreases, and ultimately $L(q = \pi)$ and $S(q = \pi)$ also start decreasing when the system enters into the non-magnetic phase with exponentially decaying spin and orbital correlations.

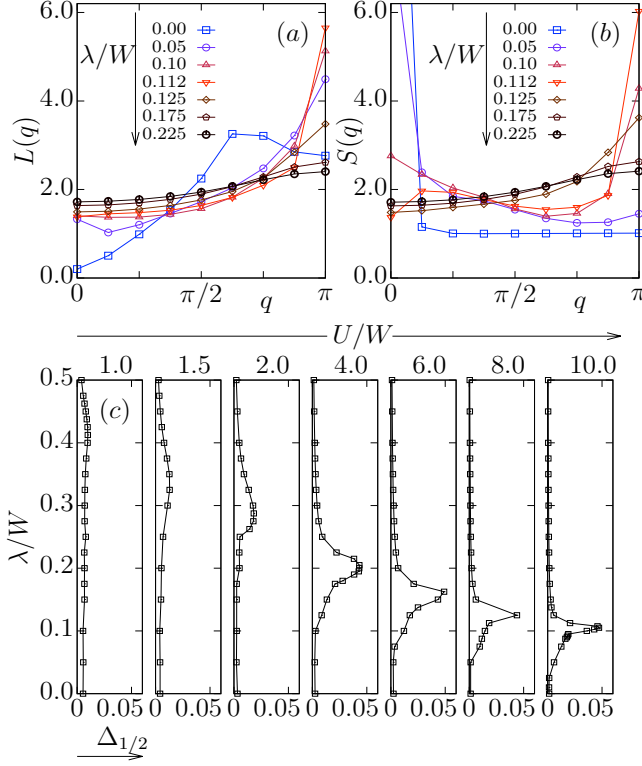


FIG. 4. Results calculated using DMRG for a one-dimensional chain of $L = 16$ sites. In panels (a) and (b), the orbital structure factor $L(q)$ and spin structure factor $S(q)$ are shown, respectively, at fixed $U/W = 10$ and for various λ/W 's. Panel (c) shows the measure of staggering in excitonic correlations $\Delta_{1/2}$ for various values of λ and U .

In our DMRG calculations, we noticed that the development of antiferromagnetic correlations in the spin and orbital channels is always accompanied by staggering in the exciton-exciton correlations, both in the intermediate and strong coupling regions. We estimate the amount of staggering in excitonic correlation for our one-dimensional chains using:

$$\Delta_m = \frac{1}{L^2} \sum_{|i-i'|>0} (-1)^{|i-i'|} \langle \Delta_{1/2,m}^{\dagger 3/2,m}(i) \Delta_{1/2,m}^{3/2,m}(i') \rangle, \quad (6)$$

where $m \in \{\pm 1/2\}$. In Fig. 4(c), the evolution of $\Delta_{1/2}$ is shown when changing λ , where each panel belongs to a different U/W . We found that smaller λ 's are needed as U/W increases to obtain staggered excitonic correlations. A finite range of λ where the excitonic correlations are staggered is present for U/W as low as 1.5, although we noticed that the magnitude of $\Delta_{1/2}$ decreases as U/W decreases, and for $U/W \lesssim 1.0$ we were unable to identify – within our numerical accuracy – the region with staggered excitonic correlations. Nonetheless, it is interesting to note that we find staggered excitonic correlations at intermediate U , where small λ shows IC-SDW metal (for evidence of metallicity see Sec. V.C). Perturbation theo-

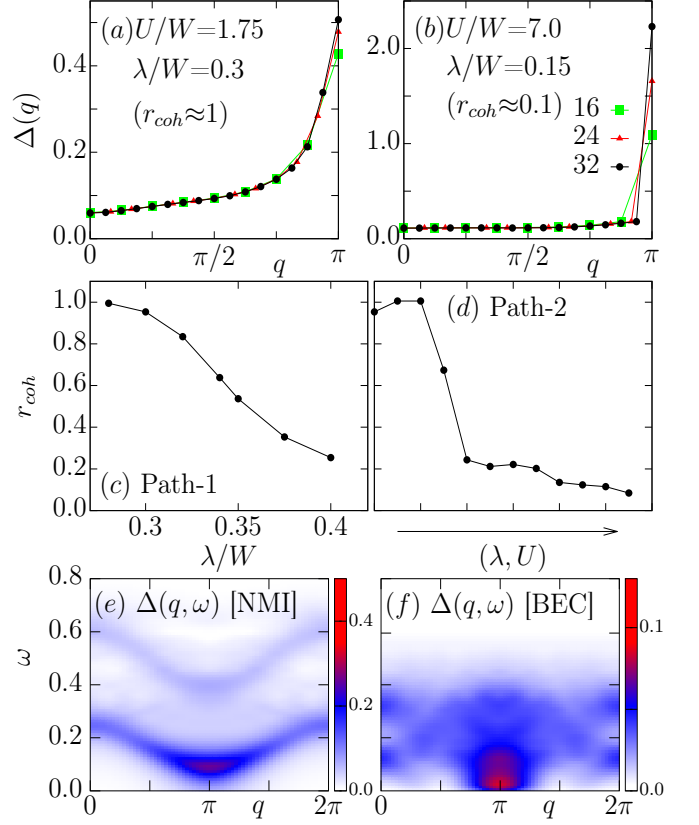


FIG. 5. Panels (a) and (b) show the momentum distribution function of excitons $\Delta(q)$ for system sizes $L = 16, 24, 32$ at two representative points of the BCS and BEC regions, respectively. Panels (c) and (d) show the coherence length for two paths inside the excitonic condensate regime, shown in the phase diagram Fig. 7. The pair-pair susceptibilities $\Delta(q, \omega)$ are shown in panel (e) at $U/W = 10$ and $\lambda/W = 0.2$ i.e. in the non-magnetic insulator (NMI) region, and in panel (f) at $U/W = 10$ and $\lambda/W = 0.11$ i.e. in the BEC region. All the calculations above were obtained using DMRG.

ries developed in the limit $U \gg t, \lambda$ cannot explain these results.

B. BCS-BEC crossover, and IC-SDW metal to BCS-Excitonic insulator transition

Now we will discuss the main result of this paper, where we present the numerical evidence for the BCS-BEC crossover in the excitonic condensate region. At intermediate U/W – the value $U/W = 1.75$ is chosen for this discussion merely for simplicity – there is a finite range of $\lambda/W \in \{0.28, 0.4\}$ where staggering in excitonic, spin, and orbital correlations is present. We calculate the coherence length $r_{coh}(m)$ using the widely-employed for-

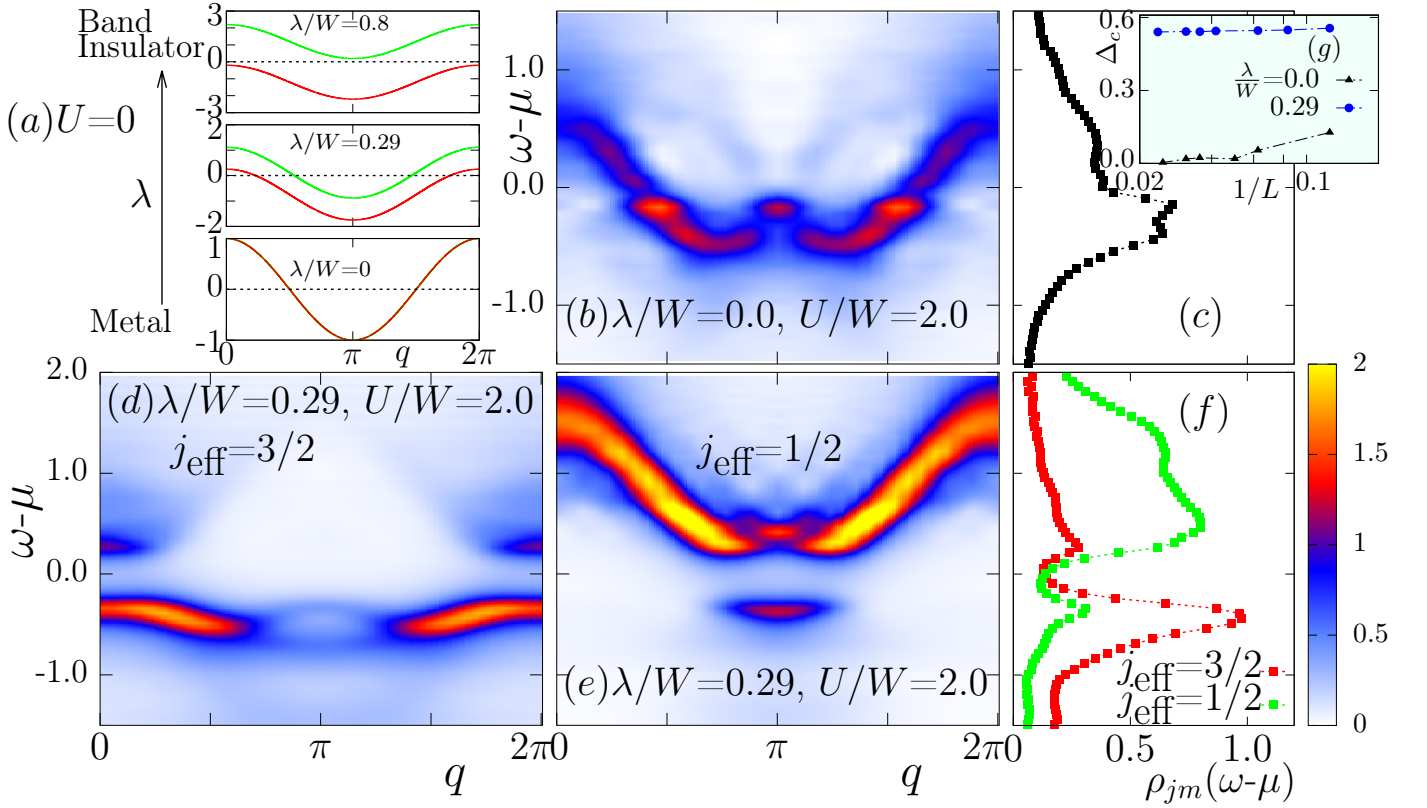


FIG. 6. The single-particle spectral function calculated using DMRG. The non-interacting band structure is shown in panel (a). Panel (b) contains $A_{jm}(q, \omega)$ for $\lambda = 0$ and $U/W = 2.0$, in the IC-SDW metallic phase. In panels (d,e) $A_{jm}(q, \omega)$ at $\lambda/W = 0.29$ and $U/W = 2.0$ is shown inside the excitonic insulator phase ($r_{coh} = 1.019$). Panels (c) and (f) show the single-particle DOS ($\rho_{jm}(\omega)$) at $\lambda = 0.0$ and $\lambda = 0.29$, respectively. The scaling of the charge gap is shown in inset (g) for ($U/W = 2, \lambda/W = 0$) and ($U/W = 2, \lambda/W = 0.29$).

mula [4, 48, 49]

$$r_{coh}(m) = \sqrt{\frac{\sum_{ij} |i-j|^2 \langle a_{i\frac{1}{2}\frac{m}{2}}^\dagger a_{j\frac{1}{2}\frac{m}{2}} \rangle}{\sum_{ij} \langle a_{i\frac{1}{2}\frac{m}{2}}^\dagger a_{j\frac{1}{2}\frac{m}{2}} \rangle}}, \quad (7)$$

where $m \in \{\pm 1/2\}$, for the points lying inside the excitonic condensate region at fixed $U/W = 1.75$, namely the Path-1 shown in Fig. 7. Note that $r_{coh}(1/2) = r_{coh}(-1/2)$. Interestingly, we found that as λ increases, r_{coh} decreases from nearly one lattice spacing $\approx a$ to $\approx 0.2a$, see Fig. 5(c). This reduction in the coherence length of electron-hole pairs resembles the BCS-BEC crossover already discussed in the context of semiconductors near the semi-metal to semiconductor transition [1–3]. We also calculate r_{coh} for various values of λ and U when transitioning from the intermediate to the strong coupling limits while being still inside the excitonic condensate region, which we call Path-2 (see Fig. 7), as shown in Fig. 5(d). Here again we found that r_{coh} decreases from $\mathcal{O}(a)$ to $\mathcal{O}(0.1a)$. The ordered $(\lambda/W, U/W)$ points chosen for Path-2 are $\{(0.3, 1.75), (0.29, 2.0), (0.29, 2.25), (0.28, 2.5), (0.24, 3.0), (0.23, 3.5), (0.21, 4.0), (0.2, 4.5), (0.17, 6.0), (0.15, 7), (0.13, 9), (0.11, 10)\}$.

In Fig. 5(a,b) we show the excitonic momentum distribution function $\Delta(q) =$

$(1/L) \sum_{i,j} \langle e^{iq(i-j)} \Delta_{1/2,m}^\dagger(i) \Delta_{1/2,m}^{3/2,m}(j) \rangle$ for two points ($\lambda/W = 0.3, U/W = 1.75$) and ($\lambda/W = 0.15, U/W = 7.0$) corresponding to the intermediate U BCS and strong U BEC regions. We found that in the BCS limit $\Delta(q = \pi)$ grows very slightly with system size L , which implies the real-space correlations of local excitons have exponential decay in this regime (see Supplementary [46]). On the other hand, in the BEC region we found nearly linearly increasing $\Delta(q = \pi)$ with L , which implies either a very slow power-law decay or even true long-range order. Such a true long-range order in our one-dimensional system is allowed as the $U(1)$ symmetry related to the excitonic condensation is explicitly broken by a finite Hund coupling [13]. The analysis above also clearly implies that as we increase the system size and hence increase the number of excitons, these excitons can condense also at momentum $q \neq \pi$ in the BCS limit, whereas in the BEC limit excitons condense only at $q = \pi$. For completeness, we would like to mention that a similar BCS-BEC crossover has also been reported in the extended Falicov-Kimball model in one-dimensional chains [7].

As discussed before, the exciton creation (electron-hole pair excitation) becomes the triplon and quintuplex ex-

citation in the atomic LS coupling limit. We calculated the excitonic pair-pair susceptibility

$$\Delta(q, \omega) = \langle \Psi_0 | \Delta_{1/2, 1/2}^{\dagger 3/2, 1/2}(q) \frac{1}{\omega + i\eta - H + E_0} \Delta_{1/2, 1/2}^{3/2, 1/2}(q) | \Psi_0 \rangle \quad (8)$$

in the strong coupling limit $U/W = 10.0$ on one-dimensional chains to study the effect of the kinetic energy. The broadening η was fixed at 0.05 eV. We choose two values $\lambda/W = 0.20$ and $\lambda/W = 0.11$ in the non-magnetic insulator and BEC regions, respectively [Figs. 5(e,f)]. We found that for the non-magnetic state, the pair-pair susceptibility shows two cosine-like bands with minima at $q = \pi$, where the lower band belongs to $\Delta J_{\text{eff}} = 1$ (triplon) and the upper band represent $\Delta J_{\text{eff}} = 2$ excitations, in agreement with previous analytical studies [27]. The BEC is expected to occur by reducing λ , when the lower band of triplons becomes gapless. In our BEC state, $\Delta(q, \omega)$ shows features very different from those in the non-magnetic state: after removing the elastic peak we found that two gapped bands appear only near $q = 0$, and the spectrum at $q = \pi$ is now gapless with emerging Goldstone-like modes. We also found continuum-like features for $q \in \{-\frac{\pi}{4}, \frac{7\pi}{4}\}$.

In the non-interacting limit, λ only splits the $j_{\text{eff}} = 3/2$ and $j_{\text{eff}} = 1/2$ bands, as shown in Fig. 6(a), driving a metal to band-insulator transition. Only in the presence of finite U the excitonic condensation happens: as shown in our DMRG results, $U/W \gtrsim 1.0$ is required to obtain a noticeable staggering in the excitonic correlations. To further investigate the excitonic condensation at intermediate U , we calculated the single-particle spectral function $A_{jm}(q, \omega)$ (see Supplementary [46]) at $U/W = 2$, using both $\lambda = 0.0$ and $\lambda/W = 0.29$ corresponding to the IC-SDW and excitonic condensate region with $r_{\text{coh}} \approx 1.0$ (BCS limit), respectively. In Fig. 6(b) we show $A_{jm}(q, \omega - \mu)$ for $\lambda = 0$: at this point all (j_{eff}, m) states are degenerate. Comparing to the band structure in the non-interacting limit, a renormalization of the bands is clearly visible, having two minima structure and a local maxima at $q = \pi$, as a consequence of the Hubbard repulsion. In this phase, we expect that the nesting vector at the chemical potential μ decides the ordering vector of the incommensurate spin-density wave. We also show the single-particle density of states $\rho_{jm}(\omega - \mu)$, see Fig 6(c), which indicates that the system has a finite density-of-states at μ suggesting this phase is metallic.

Figures 6(d) and (e) show $A_{j,m}(q, \omega - \mu)$ for $j_{\text{eff}} = 3/2$ (all $m \in \{\pm 3/2, \pm 1/2\}$ are degenerate) and $j_{\text{eff}} = 1/2$ (both $m \in \{\pm 1/2\}$ are degenerate), respectively. The gaps at μ , at wavevectors $q \approx 0$ and $q \approx \pi$ in the spectral functions of $j_{\text{eff}} = 3/2$ and $j_{\text{eff}} = 1/2$, respectively, are clearly present. These gaps appear due to the formation of bound states of electrons and holes, arising from the $q \approx 0$ and $q \approx \pi$ states of the $j_{\text{eff}} = 3/2$ and $j_{\text{eff}} = 1/2$ bands, respectively. This leads to the creation of excitons with net momentum $\approx \pi$ (indirect excitons). We also noticed a non-trivial suppression of

the spectral function near $q = \pi$ for $j_{\text{eff}} = 3/2$, below μ , but the explanation for these small features requires further work. However, it is evident that the gap opens due to the formation of indirect excitons and eventually leads to a BCS-like state. In Fig. 6(f), the j -resolved density-of-states is shown to illustrate the suppression near μ for both the $j_{\text{eff}} = 3/2$ and $1/2$ bands. A small but finite density-of-states at μ is present because of the broadening η used. To confirm the transition from metal (at $\lambda = 0$) to excitonic insulator (at $\lambda/W = 0.29$), we performed finite-size scaling of the charge gap $\Delta_c = E_G(N+1) + E_G(N-1) - 2E_G(N)$ for both points, as shown in Fig. 6(g). At $\lambda = 0.29$, using system sizes $L = 8, 12, 16, 24, 32$, and 42, we found the charge gap is quite robust 0.55 eV. Sizes $L = 8, 16, 20, 28, 32$, and 40 were used for the scaling at the $\lambda = 0$ point, which indicates that Δ_c scales to ≈ 0 eV in the thermodynamic limit.

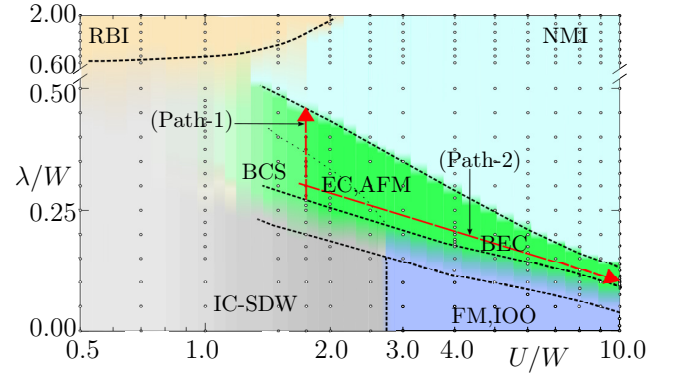


FIG. 7. λ/W vs U/W phase diagram calculated using DMRG for a one-dimensional system. The two red arrows corresponds to the paths used in panels (c,d) of Fig. 5. The vertical red arrow is chosen at $U/W = 1.75$, and depicts Path-1 of Fig. 5(c). The diagonal red arrow corresponds to the Path-2 used in Fig. 5(d). The notation RBI, IC-SDW, FM, IOO, EC, AFM, and NMI stands for relativistic band insulator, incommensurate spin-density wave, ferromagnetic, excitonic condensate, antiferromagnetic, and non-magnetic insulator, respectively.

Figure 7 ends this section by displaying the full λ vs U phase diagram for our one-dimensional systems. The CPU-costly DMRG calculations were performed for all small circles shown in the phase diagram using a system size $L = 16$. After obtaining the ground state, then spin-spin correlations, orbital-orbital correlations, and exciton-exciton correlations were calculated to analyze the properties of each phase. The (j_{eff}, m) -resolved local electronic densities were also studied to identify the relativistic band insulator phase. The dashed line inside the excitonic condensate region (green region) is only a guide to the eyes to show the BCS and BEC limits of the excitonic condensate.

V. HARTREE-FOCK RESULTS IN TWO-DIMENSIONS

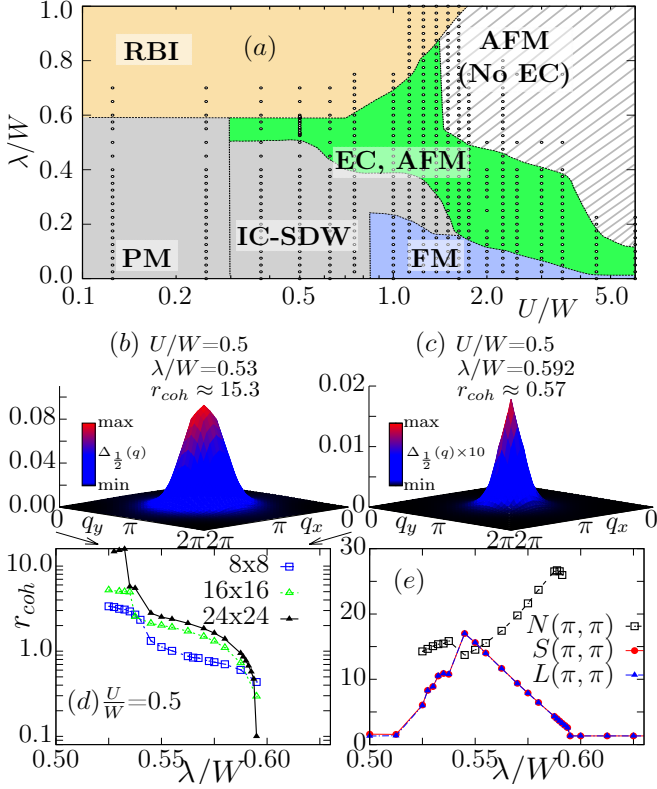


FIG. 8. Panel (a) shows the λ vs U phase diagram for the square lattice, calculated using the Hartree-Fock approximation. In panels (b) and (c), the momentum distribution function of excitons $\Delta(\mathbf{q})$ is shown at $\lambda = 0.53$ and $\lambda/W = 0.592$, respectively, for fixed $U/W = 0.5$ and a 24×24 system. The coherence length for various values of λ , at fixed $U/W = 0.5$, for system sizes 8×8 , 16×16 , and 24×24 are shown in panel (d). The $N(\pi, \pi)$, $S(\pi, \pi)$, and $L(\pi, \pi)$ are presented in (e) for various values of λ , at fixed $U/W = 0.5$ and using a 24×24 system size.

In this section, we will present and discuss the results obtained in two-dimensional lattices by performing mean-field calculations in real-space. All the four-fermionic terms in the Hubbard interaction Eq.(2) are treated under the Hartree-Fock approximation, where the single-particle density matrix expectation values $\langle c_{i\alpha\sigma}^\dagger c_{i\beta\sigma'} \rangle$ serve as order parameters at each site i (α, β are orbitals and σ, σ' are spin projection indexes). We reach self-consistency iteratively in the order parameters while tuning the chemical potential μ accordingly to attain the required electronic density. Given the many order parameters, converged results often require using 10-20 initial random initial configurations and inspecting the lowest energy achieved after the iterative process, searching for patterns that are then uniformized and test for their energy. Often also converged results at other couplings are used as seeds at new couplings, until a con-

sistent phase diagram emerges. The modified Broyden's method was used to gain fast convergence [50].

In Fig. 8(a), we show the full λ vs U phase diagram for the two-dimensional lattice. To identify the various phases, we calculated the spin structure factor and orbital structure factor on 16×16 clusters with periodic boundary conditions for all the points explicitly shown in the phase diagram. Our mean-field calculations in two dimensions capture almost all the phases found in our numerical exact one-dimensional results, the main difference being having shifted boundaries which are to be expected considering the different dimensionality and different many-body approximations. The only notable difference is that our mean-field calculations do not capture the non-magnetic phase in the strong coupling limit, because the lattice non-magnetic state can be written as a direct product of $J_{\text{eff}} = 0$ at each site i.e. $\dots |J_{\text{eff}}=0\rangle_i \otimes |J_{\text{eff}}=0\rangle_{i+1} \otimes |J_{\text{eff}}=0\rangle_{i+2} \dots$, where each $J_{\text{eff}} = 0$ state in the LS coupling limit is a sum of Slater determinants and hence cannot be reproduced by the Hartree-Fock approximation that relies on single determinants. However, the excitonic condensate phase, the focus of the present paper, is properly captured by the Hartree-Fock calculations and it is present even in a larger region of the phase diagram than in one dimension, hence giving us a good opportunity to discuss the presence of the BCS-BEC crossover in two-dimensional lattices.

To proceed with our discussion, we fix $U/W = 0.5$ ($W = 8t$) where the excitonic condensation is present in a narrow but finite range of spin-orbit coupling, while for smaller λ 's the IC-SDW phase is present. Similar to our one-dimensional DMRG calculations, in two-dimensional lattices we found that inside the excitonic condensate region (at a fixed weak or intermediate U/W values), r_{coh} decreases on increasing λ , as shown in Fig. 8(d) depicting the BCS-BEC crossover. We have calculated r_{coh} for system sizes 8×8 , 16×16 , and 24×24 . We found that in the BCS limit, r_{coh} increases as the system size increases and r_{coh} can reach values as high as $\approx 15.0a$ for the 24×24 lattice. This clearly supports our claim for the presence of the BCS state above the IC-SDW region, as in our DMRG chain calculations (but in one-dimension perhaps due to size-effects or lack of resolution, the largest r_{coh} obtained was only of order of one lattice spacing). On the other hand, we found that in the BEC limit, located below the relativistic band insulator in the phase diagram, r_{coh} is $\mathcal{O}(0.1a)$, as shown in Fig. 8(d). Figure 8(e) displays $S(\pi, \pi)$ and $L(\pi, \pi)$, for $U/W = 0.5$, to show that only for a finite range of λ the antiferromagnetic ordering develops. We also show the momentum distribution function of excitons $\Delta_{1/2}(\mathbf{q})$ at $\lambda/W = 0.53$ and $\lambda/W = 0.592$ in the BCS and BEC limits, respectively. We noticed that in the BEC limit $\Delta(\mathbf{q})$ is much sharper near $\mathbf{q} = (\pi, \pi)$ than in the BCS limit, as expected because in BEC a larger ratio of excitons is expected at the condensation momentum than other momenta. To further investigate the above claims we calculated the ratio of excitons at wavevector $\mathbf{q} = (\pi, \pi)$ and at other wavevectors

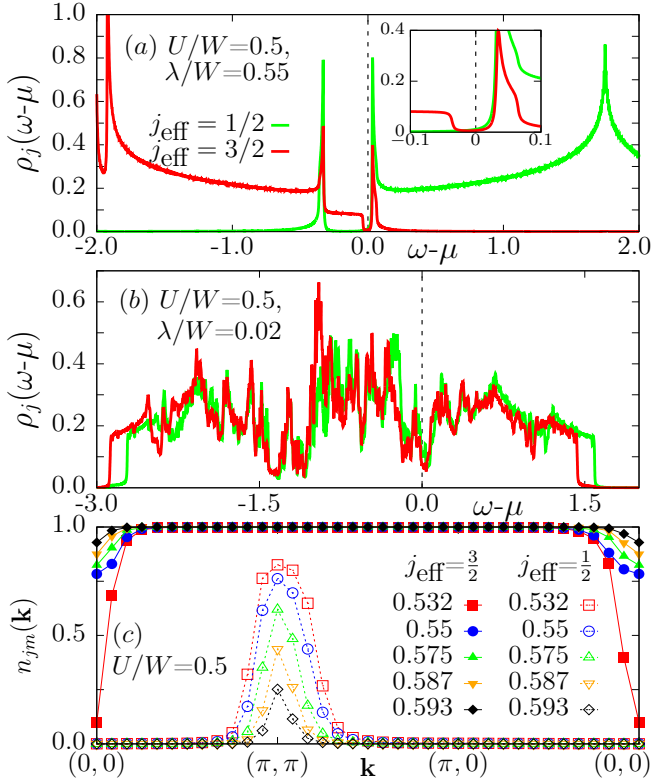


FIG. 9. The density of states, $\rho_j(\omega - \mu)$, in the Excitonic Insulator and IC-SDW regions is shown in panels (a) and (b), respectively. Panel (c) contains the momentum distribution function for electrons $n_{jm}(\mathbf{k})$ for various values of λ . $U/W = 0.5$ is fixed for all the results in the panels above. In panel (c), a system size 24×24 is used and $m = 1/2$ is fixed.

using $N(\pi, \pi) = \Delta_{1/2}(\pi, \pi) / \langle \Delta_{1/2}(\mathbf{q} \neq (\pi, \pi)) \rangle$, where $\langle \Delta_{1/2}(\mathbf{q} \neq (\pi, \pi)) \rangle = \frac{1}{L^2 - 1} \sum_{\mathbf{q} \neq (\pi, \pi)} \Delta_{1/2}(\mathbf{q})$. It is evident from Fig. 8(e) that $N(\pi, \pi)$ increases as we transition from the BCS to the BEC limits.

The single-particle density of states (DOS) provides further evidence for the existence of the excitonic condensate. Figure 9(a) and (b) show the DOS $\rho_j(\omega - \mu)$, at fixed $U/W = 0.5$. We chose $\lambda/W = 0.02$ and $\lambda/W = 0.55$ corresponding to the IC-SDW and excitonic condensate phases, respectively. As shown in Fig. 9(b), at $\lambda/W = 0.02$ a finite density-of-states at the chemical potential is present for both bands $j_{\text{eff}} = 3/2$ and $j_{\text{eff}} = 1/2$ indicating that the system is metallic in the IC-SDW phase. In the excitonic condensate phase, a small gap is present near the chemical potential in both the bands due to the condensation of excitons. The continuous distribution in eigenenergies was attained by solving 24×24 lattices with 48×48 twisted boundary conditions [51]. Two peaks arising from the small hole pocket of the $j_{\text{eff}} = 1/2$ states and electron pocket of the $j_{\text{eff}} = 3/2$ states are also visible. The inset shows the magnified $\rho_j(\omega - \mu)$ near the chemical potential. To discuss the evolution of these hole and electron pockets, as the system crossovers from the BCS to BEC limit, we show the momentum distribution

function of electrons $n_{jm}(\mathbf{k})$ in Fig. 9(c). The hole pocket is present at $\mathbf{k} = (0, 0)$ in the $j_{\text{eff}} = 3/2$ band and the electron pocket is at $\mathbf{k} = (\pi, \pi)$ in the $j_{\text{eff}} = 1/2$ band. The nesting vector between these pockets also explains the ordering momentum of the excitons. As λ increases, we noticed a gradual decrease in both electron and hole pockets which indicates that the number of carriers decreases as the system crossovers from the BCS to BEC limits.

VI. CONCLUSIONS

In this publication, we studied the degenerate t_{2g}^4 multi-orbital Hubbard model in the presence of spin-orbit coupling, using one-dimensional chains and numerically exact DMRG and also using two-dimensional clusters within the Hartree-Fock approximation. In both calculations, we provide evidence for a BCS-BEC crossover in the spin-orbit excitonic condensate, in the regime where the Hund coupling J_H is fixed at a robust value $J_H = U/4$. Within our accuracy, we established that in this model and at intermediate U/W , the system transits from an IC-SDW metallic phase to the BCS limit of an antiferromagnetic excitonic condensate, and on further increasing λ the coherence length of electron-hole pairs decreases rapidly as the system crossovers to the BEC regime. This BEC regime ends as eventually the system transits to the relativistic band insulator on increasing further λ . Our work provides the first indications of a BCS-BEC crossover in the excitonic magnetic state at intermediate U/W , a region of couplings that cannot be explored within approximations developed in the large U/W regime.

We hope our study encourages further theoretical and experimental investigations on t_{2g}^4 compounds with robust spin-orbit coupling. Although our study is performed using degenerate orbitals, we believe that our findings could be generic and relevant for materials showing magnetic excitonic condensation at intermediate values of the Hubbard repulsion and spin-orbit coupling.

VII. ACKNOWLEDGMENTS

N.K., R.S., and E.D. were supported by the U.S. Department of Energy (DOE), Office of Science, Basic Energy Sciences (BES), Materials Sciences and Engineering Division. A.N. was supported by the Canada First Research Excellence Fund. G.A. was supported by the Scientific Discovery through Advanced Computing (SciDAC) program funded by the U.S. DOE, Office of Science, Advanced Scientific Computing Research and Basic Energy Sciences, Division of Materials Sciences and Engineering. Part of this work was conducted at the Center for Nanophase Materials Sciences, sponsored by the Scientific User Facilities Division (SUFD), BES, DOE, under contract with UT-Battelle.

- ¹ D. Jérôme, T. M. Rice, and W. Kohn, *Phys. Rev.* **158**, 462 (1967); B.I. Halperin and T.M. Rice, *Rev. Mod. Phys.* **40**, 755 (1968); B.I. Halperin and T. M. Rice, *Solid State Physics* **21**, 115 (1968).
- ² N. F. Mott, *Phil. Mag.* **6**, 287 (1961).
- ³ R. S. Knox, in *Solid State Physics* (Academic Press Inc., New York, 1963), Suppl. 5, p. 100.
- ⁴ J. Kunes, *Journal of Physics: Condensed Matter*, Volume 27, Number 33 (2015).
- ⁵ C. D. Batista, J. E. Gubernatis, J. Bonca, and H. Q. Lin, *Phys. Rev. Lett.* **92**, 187601 (2004).
- ⁶ K. Sugimoto, S. Nishimoto, T. Kaneko, and Y. Ohta, *Phys. Rev. Lett.* **120**, 247602 (2018).
- ⁷ S. Ejima, T. Kaneko, Y. Ohta, and H. Fehske *Phys. Rev. Lett.* **112**, 026401 (2014).
- ⁸ K. Seki, R. Eder, and Y. Ohta *Phys. Rev. B* **84**, 245106 (2011).
- ⁹ V. N. Phan, K. W. Becker, and H. Fehske *Phys. Rev. B* **81**, 205117 (2010).
- ¹⁰ T. Sato, T. Shirakawa, and S. Yunoki, *Phys. Rev. B* **99**, 075117 (2019).
- ¹¹ A. J. Kim, H. O. Jeschke, P. Werner, and R. Valentí, *Phys. Rev. Lett.* **118**, 086401 (2017).
- ¹² N. Kaushal, J. Herbrych, A. Nocera, G. Alvarez, A. Moreo, F. A. Reboredo, E. Dagotto, *Phys. Rev. B* **96**, 155111 (2017).
- ¹³ N. Kaushal, A. Nocera, G. Alvarez, A. Moreo, and E. Dagotto, *Phys. Rev. B* **99**, 155115 (2019).
- ¹⁴ A. Kogar, M. S. Rak, S. Vig, A. A. Husain, F. Flicker, Y. Il Joe, L. Venema, G. J. MacDougall, T. C. Chiang, E. Fradkin, J. van Wezel, and P. Abbamonte, *Science* Vol. 358, Issue 6368, pp. 1314-1317 (2017).
- ¹⁵ Y. F. Lu, H. Kono, T. I. Larkin, A. W. Rost, T. Takayama, A. V. Boris, B. Keimer and H. Takagi, *Nature Communications* volume 8, Article number: 14408 (2017).
- ¹⁶ J. P. Eisenstein and A. H. MacDonald, *Nature* volume 432, pages 691-694 (2004).
- ¹⁷ G. William Burg, N. Prasad, K. Kim, T. Taniguchi, K. Watanabe, A. H. MacDonald, L. F. Register, and E. Tutuc, *Phys. Rev. Lett.* **120**, 177702 (2018).
- ¹⁸ G. Cao and P. Schlottman *Reports on Progress in Physics*, Volume 81, Number 4 (2018).
- ¹⁹ J. G. Rau, E. K.-H. Lee, and H.-Y. Kee *Annu. Rev. Condens. Matter Phys.* **7**, 195221 (2016).
- ²⁰ B. J. Kim, H. Jin, S. J. Moon, J.-Y. Kim, B.-G. Park, C. S. Leem, J. Yu, T. W. Noh, C. Kim, S.-J. Oh, J.-H. Park, V. Durairaj, G. Cao, and E. Rotenberg, *Phys. Rev. Lett.* **101**, 076402 (2008).
- ²¹ M. Souri, B. H. Kim, J. H. Gruenewald, J. G. Connell, J. Thompson, J. Nichols, J. Terzic, B. I. Min, G. Cao, J. W. Brill, and A. Seo, *Phys. Rev. B* **95**, 235125 (2017).
- ²² J. Kim, D. Casa, M. H. Upton, T. Gog, Y.-J. Kim, J. F. Mitchell, M. van Veenendaal, M. Daghofer, J. van den Brink, G. Khaliullin, and B. J. Kim, *Phys. Rev. Lett.* **108**, 177003 (2012).
- ²³ J. Kim, M. Daghofer, A. H. Said, T. Gog, J. van den Brink, G. Khaliullin, and B. J. Kim, *Nature Communications* **5**, 4453 (2014).
- ²⁴ J. H. Gruenewald, J. Kim, H. S. Kim, J. M. Johnson, J. Hwang, M. Souri, J. Terzic, S. H. Chang, A. Said, J. W. Brill, G. Cao, H. Y. Kee, and Sung S. A. Seo, *Adv. Mater.* **29** 1603798 (2016).
- ²⁵ G. Khaliullin, *Phys. Rev. Lett.* **111**, 197201 (2013).
- ²⁶ O. N. Meetei, W. S. Cole, M. Randeria, and N. Trivedi, *Phys. Rev. B* **91**, 054412 (2015).
- ²⁷ C. Svoboda, M. Randeria, and N. Trivedi, *Phys. Rev. B* **95**, 014409 (2017).
- ²⁸ G. Cao, T.F. Qi, L. Li, J. Terzic, S.J. Yuan, L.E. DeLong, G. Murthy, and R.K. Kaul, *Phys. Rev. Lett.* **112**, 056402 (2014).
- ²⁹ T. Dey, A. Maljuk, D. V. Efremov, O. Kataeva, S. Gass, C. G. F. Blum, F. Steckel, D. Gruner, T. Ritschel, A. U. B. Wolter, J. Geck, C. Hess, K. Koepf, J. van den Brink, S. Wurmehl, and B. Büchner, *Phys. Rev. B* **93**, 014434 (2016).
- ³⁰ L. T. Corredor, G. Aslan-Cansever, M. Sturza, Kaustuv Manna, A. Maljuk, S. Gass, T. Dey, A. U. B. Wolter, Olga Kataeva, A. Zimmermann, M. Geyer, C. G. F. Blum, S. Wurmehl, and B. Büchner, *Phys. Rev. B* **95**, 064418 (2017).
- ³¹ J. Terzic, H. Zheng, Feng Ye, H. D. Zhao, P. Schlottmann, L. E. De Long, S. J. Yuan, and G. Cao, *Phys. Rev. B* **96**, 064436 (2017).
- ³² S. Fuchs, T. Dey, G. Aslan-Cansever, A. Maljuk, S. Wurmehl, B. Büchner, and V. Kataev *Phys. Rev. Lett.* **120**, 237204 (2018).
- ³³ A. Nag, S. Bhowal, A. Chakraborty, M. M. Sala, A. Efimenko, F. Bert, P. K. Biswas, A. D. Hillier, M. Itoh, S. D. Kaushik, V. Siruguri, C. Meneghini, I. Dasgupta, and S. Ray *Phys. Rev. B* **98**, 014431 (2018).
- ³⁴ M. Kusch, V. M. Katukuri, N. A. Bogdanov, B. Büchner, T. Dey, D. V. Efremov, J. E. Hamann-Borrero, B. H. Kim, M. Krisch, A. Maljuk, M. Moretti Sala, S. Wurmehl, G. Aslan-Cansever, M. Sturza, L. Hozoi, J. van den Brink, and J. Geck, *Phys. Rev. B* **97**, 064421 (2018).
- ³⁵ H. Gretarsson, H. Suzuki, Hoon Kim, K. Ueda, M. Krautloher, B. J. Kim, H. Yavaş, G. Khaliullin, and B. Keimer *Phys. Rev. B* **100**, 045123 (2019).
- ³⁶ T. Feldmaier, P. Strobel, M. Schmid, P. Hansmann, M. Daghofer *arXiv:1910.13977* (2019).
- ³⁷ J. Herbrych, J. Heverhagen, N. D. Patel, G. Alvarez, M. Daghofer, A. Moreo, and E. Dagotto, *Phys. Rev. Lett.* **123**, 027203 (2019).
- ³⁸ N. D. Patel, A. Nocera, G. Alvarez, A. Moreo, S. Johnston, and E. Dagotto, *Communications Physics* volume 2, Article number: 64 (2019).
- ³⁹ J. Herbrych, N. Kaushal, A. Nocera, G. Alvarez, A. Moreo, and E. Dagotto, *Nature Communications* volume 9, Article number: 3736 (2018).
- ⁴⁰ S. R. White, *Phys. Rev. Lett.* **69**, 2863 (1992).
- ⁴¹ S. R. White, *Phys. Rev. B* **48**, 10345 (1993).
- ⁴² S. R. White, *Phys. Rev. B* **72**, 180403(R) (2005).
- ⁴³ T. D. Kühner and S. R. White *Phys. Rev. B* **60**, 335 (1999).
- ⁴⁴ A. Nocera and G. Alvarez, *Phys. Rev. E* **94**, 053308 (2016).
- ⁴⁵ H. Lu, J. R. Chamorro, C. Wan, and T. M. McQueen, *Inorg. Chem.* 2018, **57**, 22, 14443-14449 (2018).
- ⁴⁶ See Supplemental Material for the representation of spin orbit exciton operators in LS coupling limit, condensation of excitons in triplet channel, and details of DMRG spectral function calculations.
- ⁴⁷ S. Feng, N. D. Patel, P. Kim, J. H. Han, N. Trivedi, *arXiv:1912.09516* (2019).

- ⁴⁸ T. Kaneko, S. Ejima, H. Fehske, and Y. Ohta, [Phys. Rev. B **88**, 035312 \(2013\)](#).
- ⁴⁹ T. Kaneko and Y. Ohta, [Phys. Rev. B **90**, 245144 \(2014\)](#).
- ⁵⁰ D. D. Johnson, [Phys. Rev. B **38**, 12807 \(1988\)](#).
- ⁵¹ J. Salafranca, G. Alvarez, and E. Dagotto, [Phys. Rev. B **80**, 155133](#).